Deciphering how specialized interneuron-specific cell types contribute to circuit function

Alexandre Guet-McCreight[1,2] and, Frances K Skinner[1,2,3]

[1]*Krembil Research Institute, University Health Network, Toronto, ON, Canada*
[2]*Department of Physiology, University of Toronto, Toronto, ON, Canada*
[3]*Department of Medicine (Neurology), University of Toronto, Toronto, ON, Canada*

Running title: Interneuron specific cells sharpen recruitment

Corresponding Author:
Alexandre Guet-McCreight
alexandre.guet.mccreight@mail.utoronto.ca
University of Toronto

Number of pages: 33

Number of figures: 10

Number of tables: 0

Number of words Abstract: 246

Number of words Significance Statement: 119

Number of words Introduction: 642

Number of words Discussion: 1471

Conflict of Interest: The authors declare no competing financial interests.

Acknowledgements: This research was supported by the Natural Sciences and Engineering Research Council of Canada (NSERC): Discovery Grant (RGPIN - 2016 - 06182) to FKS and Graduate Scholarship (CGSD2 - 504375 - 2017) to AGM. We thank L. Topolnik for reading and providing feedback on this manuscript.

Abstract

The wide diversity of inhibitory cells across the brain makes them fit to contribute to network dynamics in specialized fashions. However, the contributions of a particular inhibitory cell type in a behaving animal is challenging to decipher as one needs to both record cellular activities and identify the cell type being recorded. Thus, using computational modeling to explore cell-specific contributions so as to predict and hypothesize functional contributions is desirable. Here we examine potential contributions of interneuron-specific 3 (I-S3) cells - a type of inhibitory interneuron found in CA1 hippocampus that only targets other inhibitory interneurons - during simulated theta rhythms. We use previously developed multi-compartment models of oriens lacunosum-moleculare (OLM) cells, the main target of I-S3 cells, and explore how I-S3 cell inputs during *in vitro* and *in vivo* scenarios contribute to theta. We find that I-S3 cells suppress OLM cell spiking, rather than engender its spiking via post-inhibitory rebound mechanisms. To elicit recruitment similar to experiment, the inclusion of disinhibited pyramidal cell inputs is necessary, suggesting that I-S3 cell firing can broaden the window for disinhibiting pyramidal cells. Using *in vivo* virtual networks, we show that I-S3 cells can contribute to a sharpening of OLM cell recruitment at theta frequencies. Further, a shifting of the timing of I-S3 cell spiking due to external modulation can shift the timing of the OLM cell firing and thus disinhibitory windows. We thus propose a specialized contribution of I-S3 cells to create temporally precise coordination of modulation pathways.

Significance Statement

How information is processed across different brain structures is an important question that relates to the different functions that the brain performs. In this work we use computational models that focus on a particular inhibitory cell type that only inhibits other inhibitory cell types – the I-S3 cell in the hippocampus. We show that this cell type is able to broaden the window for disinhibition of excitatory cells. We further illustrate that this broadening presents itself as a mechanism for input pathway switching and modulation over the timing of inhibitory cell spiking. Overall, this work contributes to our knowledge of how coordination between sensory and memory consolidation information is attained in a brain area that is involved in memory formation.

Introduction

Across the brain there is a variety of different types of excitatory and inhibitory neurons that control how information is processed (Bezaire and Soltesz, 2013; Cembrowski and Spruston, 2019; Klausberger and Somogyi, 2008; Markram et al., 2004; Pelkey et al., 2017; Tremblay et al., 2016). This diversity spans morphological, electrophysiological and molecular aspects, and examination of specific inhibitory cell types shows that there are distinct neuronal classes that can be mapped to function and behaviour (Kepecs and Fishell, 2014). However, identifying a cell type goes beyond characterization of any single genetic marker making such mappings a difficult endeavour. Explorations of inhibitory cells have additional challenges since they are typically smaller in size and are rarer than their excitatory cell counterparts, making them more difficult to record from *in vivo*. Even though there are conceptual and technical challenges in classifying cell types, it is clear, for example, that brain diseases can be specific in the cell types that they affect (Zeng and Sanes, 2017).

The CA1 hippocampus, a brain area associated with memory formation, stands out in the field by the vast amount of experimental literature characterizing its inhibitory cell types (Bezaire and Soltesz, 2013; Harris et al., 2018; Klausberger and Somogyi, 2008; Pelkey et al., 2017). Of them, we here focus on the interneuron-specific 3 (I-S3) cell type, a type of interneuron that expresses vasoactive intestinal polypeptide (VIP) and calretinin (CR). This cell type is unique in that it only inhibits other inhibitory cell types and not pyramidal cells (Acsády et al., 1996; Chamberland et al., 2010; Chamberland and Topolnik, 2012; Tyan et al., 2014; Luo et al., 2020; Guet-McCreight et al., 2020). More specifically, the primary target of I-S3 cells are oriens lacunosum moleculare (OLM) cells, a cell type that commonly expresses somatostatin (SOM) and inhibits the distal apical dendrites of pyramidal cells in CA1. Pyramidal cells represent by far the largest proportion of cells in the CA1 network (Bezaire and Soltesz, 2013; Pelkey et al., 2017). Inputs carrying "sensory-related information" from entorhinal cortex synapse onto their distal dendrites, and inputs carrying "retrieval-related information" from CA3 synapse onto their proximal dendrites (Klausberger and Somogyi, 2008; Siegle and Wilson, 2014). The OLM cells have been shown to gate sensory encoding via the inhibition of pyramidal cell distal dendrites (Leão et al., 2012; Siwani et al., 2018), and I-S3 cells are thus well placed for input-specific information gating in the CA1 area. This dis-inhibitory circuitry (i.e., I-S3 cell inhibition of OLM cells causing disinhibition of pyramidal cells) is not necessarily unique to the hippocampus since strikingly similar circuitries with VIP+ and SOM+ cell types have also been reported across several different areas of cortex (Guet-McCreight et al., 2020). Generally speaking, activation of VIP+ cells *in vivo* across different cortical areas has been associated with improved performances in a variety of different learning and memory paradigms as well as the facilitation of synaptic potentiation in pyramidal cells (Guet-McCreight et al., 2020).

In CA1, both the timing of spiking across different cell types (Bezaire et al., 2016; Klausberger and Somogyi, 2008; Mizuseki et al., 2009), as well as encoding of sensory and retrieval information (Siegle and Wilson, 2014) are known to co-occur at distinct phases of theta rhythms (4-12 Hz), which are present during movement and preparatory behaviors

(Buzsáki, 2002; Colgin, 2016). In this study, we use computational modelling to examine and compare simulated *in vitro* and *in vivo* states in OLM cells (Guet-McCreight and Skinner, 2020) so as to dissect out possible contributions of I-S3 cells in particular. We find that I-S3 cells could contribute to function by suppressing spiking in OLM cells and broadening the window for the synaptic disinhibition of pyramidal cells. Overall, our work shows that close interfacing of computational and experimental studies can help us make progress toward the challenging endeavour of mapping specialized cell types to function and behaviour.

Materials and Methods

Models of neurons and synapses, and generating in vivo-like (IVL) states

The models upon which the present work is based have been previously published. Detailed descriptions of these models with equations and parameter values can be accessed starting from Guet-McCreight and Skinner (2020). Here we provide a brief description. Two morphologically detailed multi-compartment OLM cell models, cell 1 and cell 2 (Sekulic et al., 2020), were developed in NEURON (Carnevale and Hines, 2006). Both cell models were constructed using morphological and electrophysiology data from intermediate CA1 mouse hippocampus. Code for the models is available from `https://github.com/FKSkinnerLab/OLMng`. Ion channel mechanisms include: hyperpolarization-activated cation channels (H), transient sodium (NaT), fast and slow delayed rectifier potassium ($Kdrf$, $Kdrs$), A-type potassium (A), M-type potassium (M), T- and L-type calcium (CaT, CaL), and calcium-dependent potassium (KCa) channels. All of these mechanisms are distributed throughout the cell, with CaT, CaL, and KCa being inserted only in dendritic compartments, the rest inserted in somatic and dendritic compartments, and NaT, $Kdrf$, and $Kdrs$ also being inserted in axonal compartments. We refer to currents generated by the different ion channel mechanisms with subscripts. The two OLM cell models were developed using the same biological OLM cell for each model, and are the most up-to-date OLM cell models currently available (Sekulic et al., 2020). Although each of these models represent OLM cells as captured by mimicking the electrophysiological recording outputs from the particular biological cell, they differ in their detailed morphologies and conductance values for each of the various ion channel mechanisms. Throughout the paper we use both models so as to consider whether these differences would affect our results.

For the synapse model we use NEURON's built-in Exp2Syn function. The input populations to OLM cells include: I-S3 cell inputs, GABAergic long-range projecting inputs from medial septum (MS), bistratified cell inputs (BIS), and local pyramidal (PYR) cell inputs [I-S3 cells & MS: see Chamberland et al. (2010); BIS & PYR cells: see Leão et al. (2012)]. In the absence of specific constraints, these inputs are distributed randomly across all dendritic compartments. OLM cells also receive inputs locally from long-range projecting VIP+ cells in CA1 (Francavilla et al., 2018), though because these cells are silent during theta rhythms, we did not include them in this study. In previous work, we had performed optimizations of synaptic conductances across dendritic compartments so as to estimate the

weights for each input type. We obtained increasing values with distance from soma (G_{PYR} = 0.00020 to 0.00082 μS; G_{MS} = 0.00024 to 0.00132 μS; G_{I-S3} = 0.00018 to 0.00068 μS; G_{BIS} = 0.00021 to 0.00100 μS). Consideration of other inputs and further details can be found in Guet-McCreight and Skinner (2020).

In previous work using I-S3 cell models (Guet-McCreight and Skinner, 2019), we had developed an approach for performing high-resolution parameter searches in parallel on the Neuroscience Gateway (NSG) for high-performance computing (Sivagnanam et al., 2013) to find synaptic input parameter combinations (i.e. excitatory and inhibitory numbers of synapses and spike rates) that could generate *in vivo*-like (IVL) states. In Guet-McCreight and Skinner (2020) we did the same for OLM cells. IVL states resulted in synaptic parameter values for cell 1 of 1268 excitatory synapses firing at 1.6 Hz and 1254 inhibitory synapses firing at 8.7 Hz, and for cell 2, 1503 excitatory synapses firing at 1.5 Hz and 1532 inhibitory synapses firing at 8 Hz, distributed throughout the dendritic tree.

Approaches and data analyses

To investigate the experimental results from Tyan et al. (2014), we use a similar protocol in our computational models where we first depolarize the cell model enough to attain a spike rate of 7.25 Hz. We then activate select input populations at different frequencies in our models. The synaptic locations for the inputs are chosen randomly across the dendritic arbour of OLM cells (**Fig. 2**), as was done previously (Guet-McCreight and Skinner, 2020). Although we look at a variety of different input schemes to gauge possible contributions of different network components, we focus on displaying results that explore the contributions from I-S3 cell inputs.

To compute the phase response ($\Delta\Phi$; **Fig. 4B**), we obtain the interspike interval of the two spikes preceding the perturbation ($T0$) and the interspike interval between the last spike preceding the perturbation and the first spike following the perturbation ($T1$). We calculate the phase response as follows:

$$\Delta\Phi = \frac{T1 - T0}{T0} \times 100 \tag{1}$$

In this sense, the phase response is normalized to 1 and converted to a percent. A negative value means a phase advance, or a shortening of the interspike interval. A positive value means a phase delay, or a lengthening of the interspike interval. To compute the change in currents (i.e. same calculation used for each current type; **Fig. 4C**) caused by the perturbation, we obtain the peak current amplitude generated in the period from the 2nd last spike preceding the perturbation to the perturbation time ($I0$), and the peak current amplitude generated in the period from the perturbation time to the 2nd spike following the perturbation ($I1$). Percent change in peak current is calculated as follows:

$$\Delta I = \frac{I1 - I0}{I0} \times 100 \tag{2}$$

As such, positive values indicate percent increases in peak current amplitude, and negative values indicate percent decreases in peak current amplitude.

To examine spiking resonance in *in vitro* states, we generate 50 different baseline spike rates in our OLM models by applying a range of holding currents from 30-152.5 pA (cell 1) and 22-144.5 pA (cell 2) - note that plots of the frequency-current relationships of these models have been reported previously (Guet-McCreight and Skinner, 2020). This elicits a range of baseline spike rates from about 1-35 Hz in both models. Each of these models is then subjected to a range of inputs at different input frequencies (0.5 - 30 Hz) to determine spike resonance frequencies.

To examine spiking resonance in *in vivo* states, we also generate 50 different baseline spike rates in our OLM models. However, this is done by changing the random seed that controls placement of synapses and presynaptic spike times, rather than by changing the holding current since this is not what would be the case *in vivo*. This also generates different spike rates (across random seeds), though not with as wide of a range as changing the holding current in the *in vitro* case. We obtain 50 baseline spike rates by using 50 different random seeds.

For all of these models, we compute the baseline spike rate (f_B) and power spectral density (PSD) of the spike train (1's for spikes and 0's for no spikes). The PSD is computed in python using the welch function available as part of the scipy module: `signal.welch(signal, fs=1/dt, scaling='density', nperseg=20000)`. We then apply a series of different input frequencies (f_I), and using different input populations, and the PSD is computed following each input frequency. The different input populations (left to right in **Fig. 5**) are: 30 frequency-modulated I-S3 cell inputs, 30 frequency-modulated PYR cell inputs, and 30 frequency-modulated inputs from each input populations (i.e. I-S3, MS, BIS, and PYR cells), with start time delays from each other based on their relative timing during theta rhythms (Bezaire et al., 2016; Hangya et al., 2009; Luo et al., 2020). Specifically, these start times (phases) relative to a 125 ms theta cycle are the following: I-S3, 45°; MS, 225°; BIS, 270°; PYR, 270 °. We note that the choice to use 30 I-S3 synapses is because at this number of synapses, I-S3 cell synaptic activation can exhibit a sufficient level of synaptic control over OLM cell spiking at 5 Hz in both models (**Fig. 3A**). The choice to use the same numbers of PYR cell, MS cell, and BIS cell synapses is simply to keep the numbers equivalent in the absence of appropriate experimental data obtained in this context to constrain these numbers.

To gauge spike frequency resonance, we use a ratio to baseline measurement (i.e. 'baseline ratio' or δPSD), which is computed by dividing the PSD at the f_I by the PSD at the f_I in the corresponding baseline trace (i.e. without the modulatory inputs):

$$\delta PSD = \frac{PSD_{f_{I_{modulated}}}}{PSD_{f_{I_{baseline}}}} \tag{3}$$

In other words, it is a measurement of how much the PSD at the f_I changes relative to baseline once modulatory inputs are added. A value of 1 would therefore indicate that there is no change in PSD, values less than 1 indicate a decrease in PSD, and values greater than 1 indicate an increase in PSD.

Results

In the CA1 hippocampus, there are four known types of interneuron-specific (I-S) cells, interneurons that are specialized to primarily target other interneurons. In particular, VIP/CR+ I-S3 cells have OLM cells as their primary target. Given this, we take advantage of our computational models and approaches to examine I-S3 cell contributions in hippocampal circuits from the perspective of I-S3 cell control over OLM cell spiking.

I-S3 cell control over OLM cell spiking - multiple possibilities

In vitro, optogenetic activation of CR+ cells, which includes I-S3 cells, can preferentially control the timing of OLM cell spiking at 5 and 10 Hz, but not 1 and 20 Hz. Tyan et al. (2014) considered that this was achieved through post-inhibitory rebound (PIR) spiking mechanisms. However, because other inhibitory synapses and excitatory synapses were not blocked in these experiments, it is unclear whether this is primarily due to network effects or to intrinsic OLM cell properties that promote PIR spiking. As well, it is unknown whether and how these *in vitro* findings would translate to similar contributions in a behaving animal. Targeting and dissecting out the contributions of I-S3 cell inputs to OLM cell spiking *in vivo* would be technically difficult experiments to perform. OLM cells exhibit prominent sag currents which are due to hyperpolarization-activated cation channels (h-channels) (Maccaferri and McBain, 1996; Sekulic et al., 2020; Zemankovics et al., 2010), and can promote PIR spiking (Ascoli et al., 2010). H-channels are also thought to contribute to spike resonance properties in OLM cells *in vivo* at theta frequencies, but this has only been tested *in vitro* using dynamic-clamp experimental techniques (Kispersky et al., 2012), as well as *in silico* using multi-compartment modelling (Sekulić and Skinner, 2017). *In vitro*, OLM cells phase-lock well to theta frequency-modulated inputs, and this finding is independent of whether h-channels are blocked (Kispersky et al., 2012). However, since the dynamic-clamp experiments injected synaptic currents at the soma, possible contributions of dendritic h-channels could not be assessed. This was more fully explored in a modeling study that used somatodendritically distributed synapses on OLM cell multi-compartment models to simulate *in vivo*-like states in the presence or absence of dendritic h-channels (Sekulić and Skinner, 2017). It was found that there was a shift in spike resonance from high to low theta frequencies if, respectively, dendritic h-channels were present or not (Sekulić and Skinner, 2017). Here, with our state-of-the-art OLM cell models and explicit *in vivo*-like states, we can explore this specifically from I-S3 cell perspectives.

There are several ways in which I-S3 cells could manifest their control over OLM cells. If it is primarily through PIR spiking, this would imply that inhibitory perturbations from I-S3 cells to OLM cells would essentially speed up the onset of a spike (**Fig. 1A**), due to intrinsic OLM cell mechanisms such as I_H, I_{CaT}, and I_M that would interact with the incoming inhibitory perturbations. However, there are other ways in which I-S3 cells could have an effect on OLM cells in the hippocampal circuitry. I-S3 cells could be controlling the timing of OLM cell spiking by suppressing spikes that would occur between OLM cell's spiking otherwise (**Fig. 1B**). This would require OLM cells to be spiking

faster than the frequency at which I-S3 cells are activated to exert their control. Since during the *in vitro* experimental recordings (Tyan et al., 2014), the average spike rate of the OLM cells is 7.3 Hz and OLM cells could be recruited to spike at 10 Hz photo-activation patterns, this is unlikely to be the case. In either case, whether inhibitory inputs alone can suppress spiking or cause PIR spiking, depends on specific conductance densities and the interplay between different conductances. It is also possible that photoactivation of I-S3 cells might also have the general effect of disinhibiting PYR cells (**Fig. 1C**), which could then further phase lock the spiking of OLM cells through recurrent excitation. We note that there are additional ways in which I-S3 cells could control OLM cell spiking that involve other cell types. That is, it is possible that inhibition of BIS cells by I-S3 cell activation could contribute towards disinhibiting PYR cells, which could further augment recurrent excitation to OLM cells in an 'I-S3 to BIS to PYR to OLM cell' type pathway. It is also possible that inhibition of BIS cells could contribute to additional inhibition of OLM cells in an 'I-S3 to BIS to OLM cell' type pathway. Since we are examining virtual networks from an OLM cell perspective, these additional pathways cannot be directly explored in our simulations. However, these additional possibilities are essentially enhancements to the three scenarios shown in **Fig. 1** that we do consider.

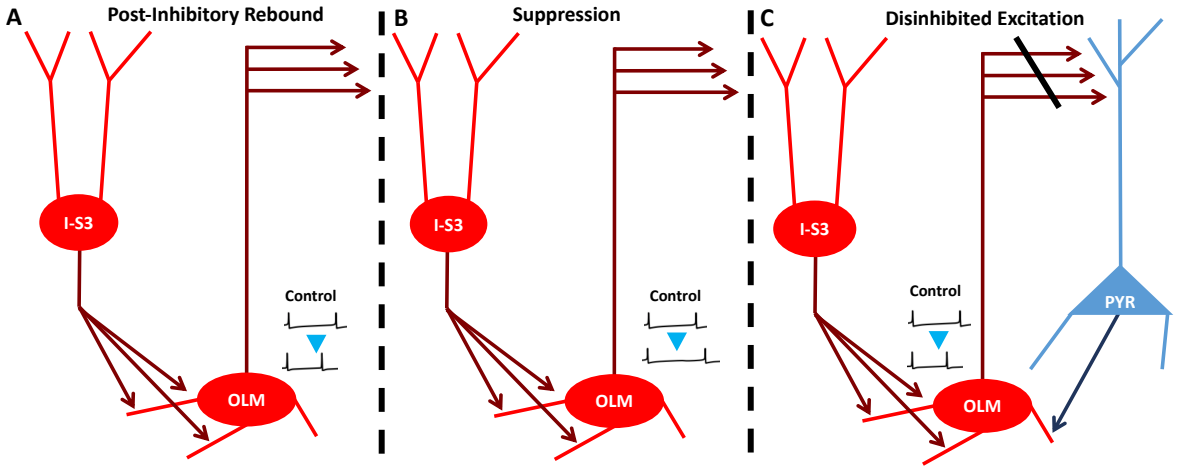

Figure 1. Potential mechanisms through which I-S3 cell activation can control OLM cell spiking. A: I-S3 cell inputs can time the activity of OLM cells through inhibitory perturbations that generate post-inhibitory rebound (PIR) spiking. **B:** I-S3 cell inputs can suppress spikes and time OLM cell spiking by lengthening their interspike intervals. **C:** I-S3 cell inputs can lead to disinhibition of PYR cells such that they can directly excite OLM cells to spike.

I-S3 cell input populations alone do not fully entrain OLM cell spiking

Let us first examine how I-S3 cell synaptic inputs alone could control OLM cell output. Here we used optimized synaptic parameters in each compartment of the OLM cell models (Guet-McCreight and Skinner, 2020) so as to capture the amplitudes and kinetics previously reported experimentally for MS and I-S3 cell inputs (Chamberland et al., 2010), as well as BIS and PYR cell inputs (Leão et al., 2012). For a full description of this methodology, see

Guet-McCreight and Skinner (2020). An example of I-S3 cell synaptic input distributed on the OLM cell models is shown in **Fig. 2A**. We apply I-S3 cell synaptic inputs alone with rhythmic spiking at 1 Hz, 5 Hz, 8 Hz, 10 Hz, and 20 Hz and using 0 to 60 synapses. Resulting output from OLM cell models is shown in **Fig. 3A**. In looking at the spike traces across both cell 1 and cell 2, entrainment by the I-S3 cell synapses occurs primarily at 5 Hz when there is a large enough number of frequency-modulated synapses. At higher frequencies, however, I-S3 cell inhibitory synapses only lead to spiking on every other cycle. For example, at 10 Hz stimulation with 30 I-S3 cell synapses, the OLM cell models spike at 5 Hz. This is in stark contrast with the experimental results that show that OLM cells spike at 10 Hz when receiving 10 Hz inhibition from CR+ cells (Tyan et al., 2014). This suggests that I-S3 cell synapses could delay the spiking of OLM cells on each cycle, which is contrary to what one would expect if PIR mechanisms in OLM cells were playing a large part. That is, the simulations indicate that I-S3 cells cause phase-delays and not phase-advances of OLM cell spiking. We also tested the inclusion of other inhibitory populations [e.g. MS cell inputs, which were reported by Chamberland et al. (2010) to have comparatively larger IPSC amplitudes than I-S3 cell inputs], as well as clustering I-S3 cell synapses on distal or proximal dendrites [i.e. since I-S3 cell IPSC amplitudes from Chamberland et al. (2010) suggest preferred distal localization of I-S3 cell synapses], and these manipulations did not lead to better spike entrainment at 10 Hz frequencies (not shown). We note that IPSP magnitudes are comparable (**Fig. 3D**) to those generated experimentally during wide-field optogenetic stimulation of CR+ cells (Tyan et al., 2014). However, this blown-up trace also highlights that the amplitude of IPSPs are dependent on their timing relative to the after spike hyperpolarization portion of the trace, which causes reduced IPSP amplitudes.

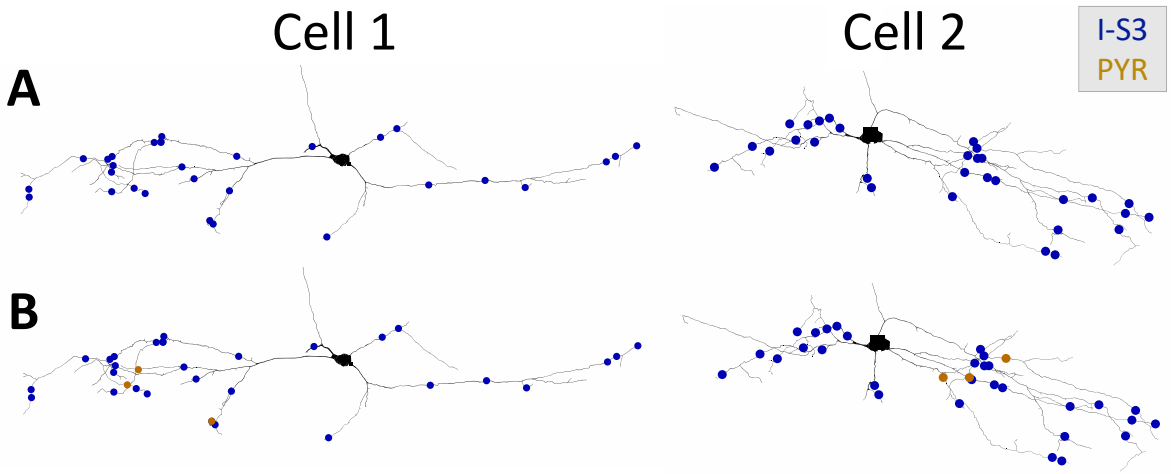

Figure 2. Example locations of synaptic inputs. A: Example synaptic locations of 30 I-S3 cell inputs. **B:** Example synaptic locations of 30 I-S3 cell inputs and 3 PYR cell inputs.

If we also include a few frequency-modulated PYR cell synapses (i.e. enough to generate spiking) on the OLM cell models (see **Fig. 2B**), we could obtain the level of spike entrainment (**Fig. 3B & E**) previously seen in experiment (Tyan et al., 2014). However, this entrainment is strong up to 20 Hz as well, which is unlike what is seen experimentally

(Tyan et al., 2014). The inclusion of frequency-modulated inputs from both I-S3 and PYR cells is 'virtual', meaning that we are not explicitly modelling I-S3 and PYR cells in a circuit configuration with the OLM cell models. That is, our virtual network simulations assume that PYR cells will spike at 20 Hz as there is no explicit modeling of tri-synaptic connectivity between I-S3 cells, OLM cells, and PYR cells. Thus a possible interpretation is that while the modeling cannot differentiate between the different frequency-modulated synapses, experimentally, photo-activation of CR+ cells at 20 Hz may not lead to PYR cell spiking at 20 Hz by disinhibition (**Fig. 1C**) to influence OLM cells at these higher frequencies. Additionally, wide-field optogenetic stimulation of CR+ cells in Tyan et al. (2014) was often capable of generating 2-3 OLM cell action potentials. This effect was not captured when scaling up I-S3 cell inputs alone (**Fig. 3A**) or with a minimal number of PYR cell inputs (**Fig. 3B**). In scaling up the number of PYR cell inputs, however, we find that this effect can be replicated (**Fig. 3C & F**). As such, our simulations suggest that wide-field activation of CR+ cells, that includes I-S3 cells, disinhibits a large enough number of PYR cells to cause a robust recruitment of OLM cells to spike.

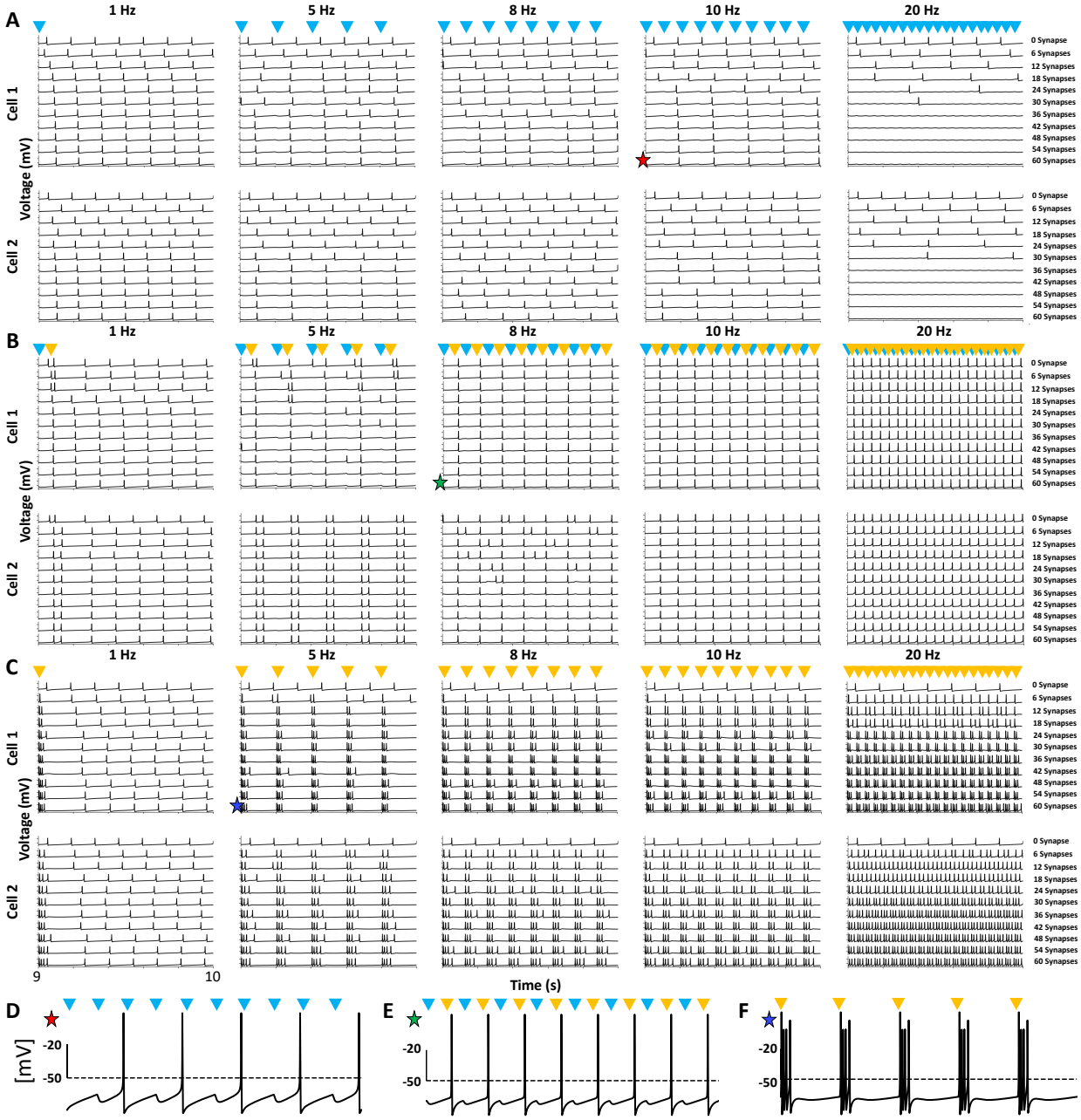

Figure 3. I-S3 cell inputs alone cannot elicit PIR spiking in OLM cells at higher than baseline spike rate frequencies. A: Simulated voltage traces in the 9-10s simulation times across several frequency-modulated I-S3 cell inhibitory frequencies (left to right) and numbers of I-S3 cell synapses (top to bottom). Blue arrows indicate times when I-S3 cell synapses are activated. For each voltage trace axis, the two notches indicate voltages of -50 mV and 0 mV. **B:** Same as in A but with inclusion of 3 PYR cell inputs (timing indicated by the yellow arrows). Note that this number of PYR cell inputs is fixed across simulations. **C:** Same as in A but with a scaling up of PYR cell inputs alone instead of I-S3 cell inputs alone. **D-F:** Blown up versions of the traces highlighted by the stars in A-C, respectively.

Inhibitory perturbations rarely elicit post-inhibitory rebound (PIR) spiking

To further unpack why the OLM cell models do not exhibit phase advancements in response to inhibitory perturbations, we turn to phase response curves (PRCs). PRCs are used in studies of oscillatory systems such as neuronal spiking (Rinzel and Ermentrout, 1989; Schultheiss et al., 2011). Specifically, they are used to indicate the change in the cycle period as a function of the phase at which a perturbation is received, thus predicting its response to rhythmic inputs. In the case of a spiking neuron, this would therefore be a change in the interspike interval. We compute the PRCs at two baseline spike rates in the OLM cell models (just past rheobase and 7.25 Hz) and use 30 I-S3 cell synapses spread randomly across the dendritic tree as the inhibitory perturbation (**Figs. 2A** and **4A**). Across these two different baseline spike rates, phase delays are almost always present in response to inhibitory perturbations, with the smallest phase delay occurring when the perturbation is during the spike refractory period, and the largest phase delay occurring when the perturbation is just before spike threshold (**Fig. 4B**, 7.25 Hz). At the lower baseline spike rate (**Fig. 4B**, rheobase), phase advances can occur when the perturbation occurs at near 40% of the interspike interval, however these are small phase advancements (negative values), and only occur with cell 1, and not with cell 2.

With our OLM cell models in hand, we can also examine perturbation phase-dependent shift in amplitudes of the different currents from the various ion channel mechanisms including I_H, I_M, I_{CaL}, I_{CaT}, and I_{K_A}. This is shown in **Fig. 4C** at two different OLM cell firing frequencies. Specifically, at frequencies observed experimentally (7.25 Hz; two lower plots), we obtain phase-dependent increases in I_H (cyan), and I_{CaL} (yellow), and decreases in I_M (purple), which should all enhance the likelihood of PIR spiking (i.e. more inward current and less outward current). We note that in all cases maximal I_{CaT} (grey) is decreased following the inhibitory perturbation, regardless of the perturbation phase, but is steadily decreased less at later phases of the interspike interval. A phase-dependent increase, albeit a small one, in I_{K_A} (blue), however, would counteract rebound firing since I_{K_A} is known to suppress PIR spiking (Ascoli et al., 2010). It should be noted that contributions from I_{K_A} are large in these models, which could partially account for the lack of inhibitory perturbation-dependent phase advances. Other currents (I_{Kdrf}: orange, I_{Kdrs}: green, I_{KCa}: red, I_{Na}: pink, I_L: brown) did not show appreciable inhibitory perturbation phase-dependent changes in maximal magnitude.

At the lower baseline spike rates however (i.e. near rheobase; **Fig. 4**, top two plots), only the I_H current shows an appreciable perturbation phase-dependent shift in amplitude, with the peak amplitude occurring when the perturbation is at 40% of the interspike interval, which corresponds to the perturbation timing that can cause phase advancements. These results suggest that PIR mechanisms that can lead to phase advances in OLM cells will primarily be mediated by I_H activation, and only when the OLM cell is spiking at the lower spike rates. Possibly, large perturbation-dependent enhancements in contributions from I_{K_A} contribute towards the prevention of phase advances from occurring more broadly across higher spike rates. Since I_{K_A} phase-dependence near rheobase is flat compared to at higher spike rates, this may also account for why some phase advances are permitted near rheobase. Though there is a difference in PRCs across the two models at lower baseline spike rates, the ion channel current responses are consistent. One potential

reason for the difference is a lower I_H output in cell 2 compared to cell 1 (**Fig. 4C**), which would explain why phase advances at lower baseline spike rates could be seen in cell 1 but not cell 2. Altogether, these results suggest that inhibitory inputs alone, via I-S3 cells, are not sufficient to elicit PIR mechanisms in OLM cells. Rather, the modeling predicts that I-S3 cell activation suppresses OLM cell spiking (i.e. causing spike phase delays), which in turn would allow disinhibition of PYR cells which could then entrain OLM cell spiking through recurrent excitation.

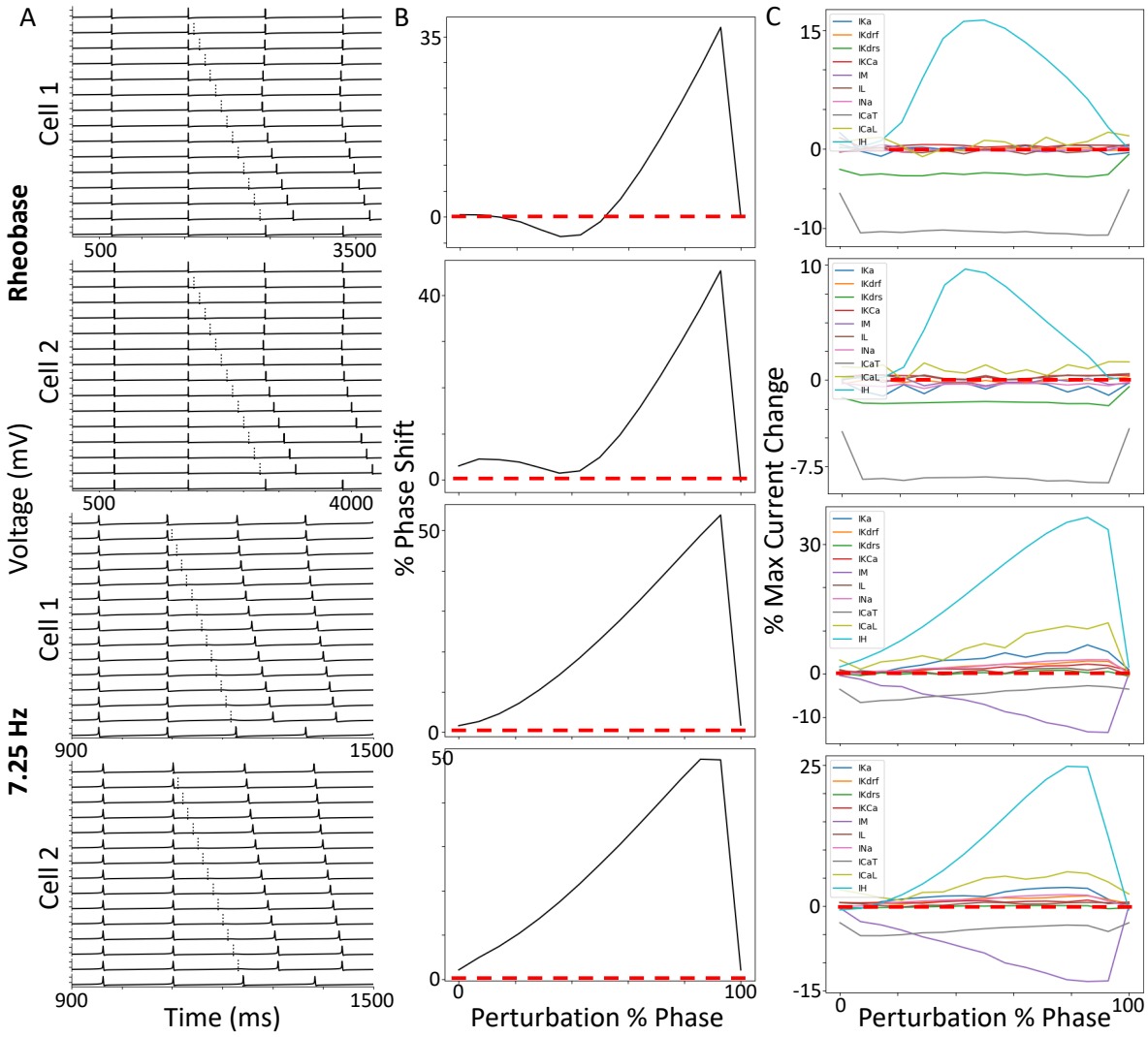

Figure 4. Inhibitory perturbations alone mostly just cause phase delays in OLM cell models. A: Voltage traces (the two notches on each y-axis are -50 mV and 0 mV) illustrating the phase response curve protocols at two different baseline frequencies (rheobase and 7.25 Hz), where the inhibitory perturbation (30 I-S3 cell synapses indicated by the dashed line in each trace), is moved from earlier (0%) to later (100%) phases of an interspike interval cycle. **B**: Resulting PRCs where more positive phase shifts indicate larger phase delays. **C**: Perturbation phase-dependent changes in peak current amplitude for each ion channel present in the model. Currents are colored as follows (same order as in legend): I_{K_A} (blue), I_{Kdrf} (orange), I_{Kdrs} (green), I_{KCa} (red), I_M (purple), I_L (brown), I_{Na} (pink), I_{CaT} (grey), I_{CaL} (yellow), and I_H (cyan). In these plots, I_H (cyan) shows the largest phase-dependent increases in maximal current magnitude. The dashed red line indicates the zero line in B and C plots. The measurements shown here are extracted from current traces obtained from the first dendritic compartment adjacent to the soma since calcium channels are not present in the somatic compartments.

In vitro spike resonance is dependent on baseline spike rate

So far we have limited our explorations to a few input frequencies and baseline spike rates based on previous experimental explorations (Tyan et al., 2014). However, from analyzing these results it is clear that inhibitory modulation is strongly dependent on the baseline firing rate of the OLM cell (f_B), as well as the frequency of the incoming frequency-modulated synaptic inputs (f_I), though the precise relationship between the two is unclear. In this section we unpack this question by incrementally changing the holding current to elicit different baseline spike rates (i.e. 1-35 Hz), while at the same time submitting the model at each holding current to a barrage of different input frequencies. We note that this range of baseline spike rates approximately spans the range of spike rates that have been reported for OLM cells *in vivo* across different behavioral and network states (Katona et al., 2014; Varga et al., 2012). In this way we can establish a 'ground-truth' regarding preferred output responses of OLM cells in the face of various input frequencies, i.e., an OLM cell spiking resonance, given different baseline spike rates in an *in vitro* context. After this, we will turn to examining what OLM cell spike resonance might look like in an *in vivo* context. The *in vitro* context simply means that the OLM cells are not bombarded with excitatory and inhibitory synaptic inputs and we simply apply the various holding currents to the somatic compartment and rhythmic putative synaptic input activations on dendritic compartments due to potential optogenetic experiments.

In **Fig. 5A1-C1** we show the spike resonant frequencies (f_R) of OLM cells when receiving inhibitory inputs from I-S3 cells, or excitatory inputs from PYR cells, or inputs from all populations (i.e. including MS and BIS inputs). We define f_R as the input frequency generating the largest baseline ratio. When receiving only I-S3 cell inhibitory inputs, f_R is largely dependent on f_B. That is, if the OLM cell is firing at a higher rate, then f_R is also higher. This can be seen more clearly in **Fig. 5A2**, which also highlights that f_R can also occasionally be larger than f_B, despite having spike rates at f_R that are always suppressed compared to f_B (**Fig. 5A3**; i.e. consistent with the phase delays due to inhibitory perturbations reported in previous sections). One explanation for this is that when the baseline ratio is enhanced in those cases, the spikes that are being suppressed are spikes that occasionally fall in phase with the modulatory inputs. In this sense, the modulatory inhibitory inputs are keeping the spiking entrained through suppression. This can happen regardless of whether f_R is greater than or lesser than f_B, and depends on how the intrinsic spike train aligns with the modulatory input spike trains.

Overall, these results make sense given the findings from the previous section showing that I-S3 cell synapses alone do not reliably cause phase advances. Specifically, recruitment of OLM cell spiking to certain inhibitory input frequencies is largely baseline spike rate-dependent because inhibitory perturbations mostly just cause phase delays. For example, if the baseline spike rate is much smaller than the input frequency, inhibitory perturbations will only cause suppression of spikes, and the PSD at the input frequency is more likely to drop. Likewise, if the baseline spike rate is much larger than the input frequency, then inhibitory perturbations will have minimal effects on spiking, as they may only suppress a small fraction of spikes. Thus, the spike resonant frequency is therefore largest when the baseline spike frequency is

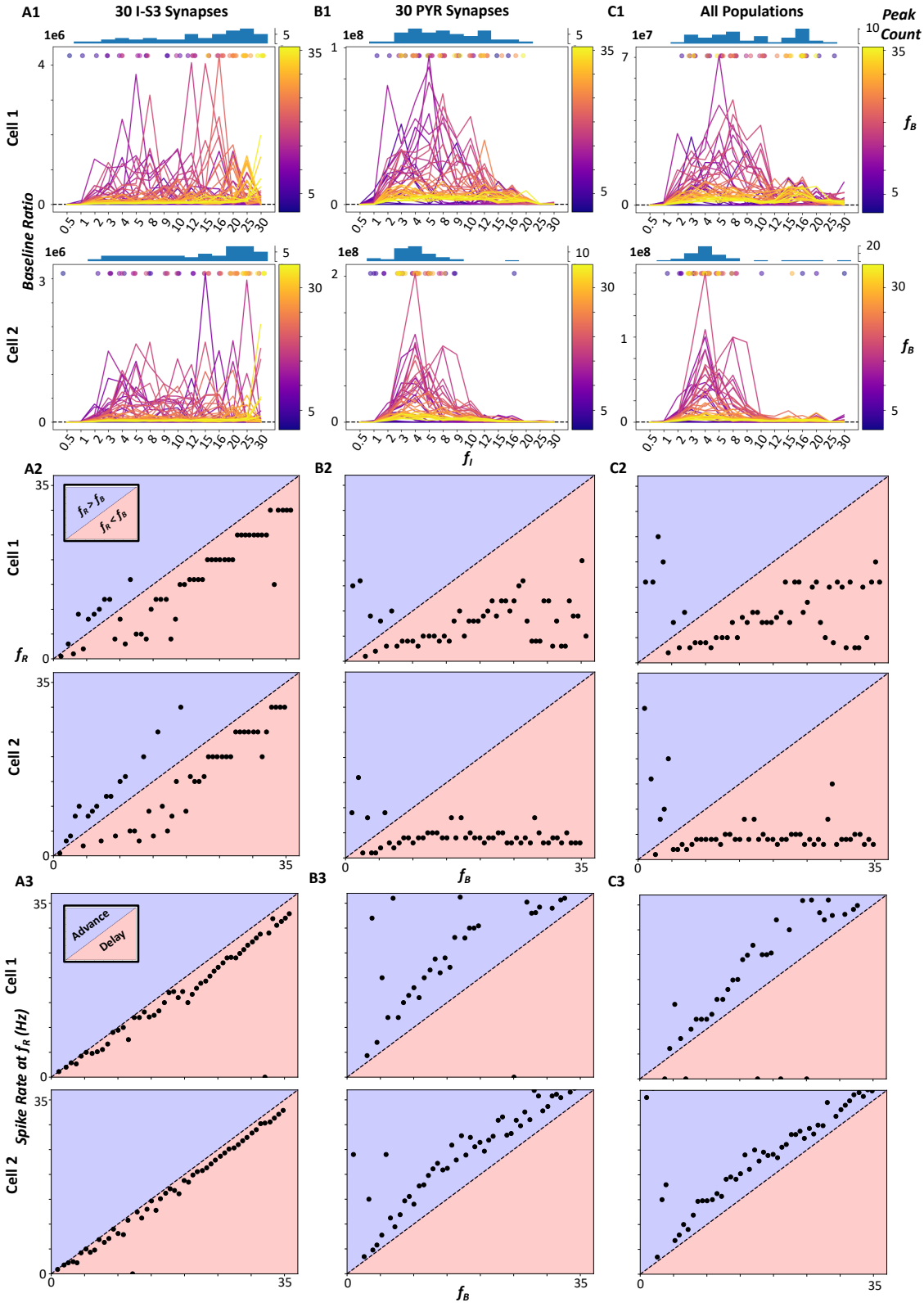

Figure 5. ***In vitro*** **spike resonant frequency of OLM cell models due to inhibitory inputs, but not excitatory inputs, is dependent on the baseline spike rate.**

(Continued) A1-C1: Baseline ratios (**A:** I-S3 cell inputs, **B:** PYR cell inputs, **C:** a combination of all inputs) computed across different modulation frequencies, f_I, and different holding currents (as shown by the range of different baseline frequencies, f_B, indicated by the colorbar). The colored dots plotted above the traces indicate the peak/resonant frequency (the color corresponds to the f_B) and the histograms above the plots show the distributions of peak/resonant frequencies across holding currents and input frequencies. The dashed black lines indicate a baseline ratio of 1 (note that the y-axis scale is large, so this line appears very close to 0), i.e. the point at which the PSD before and after applying modulatory inputs does not change. Values larger than 1 indicate an increase in the PSD, and values smaller than 1 indicate a decrease in the PSD. **A2-C2**: Resonant frequencies, f_R, plotted against f_B. Dots in blue areas indicate simulations where f_R is greater than f_B, and dots in red areas indicate simulations where f_R is less than f_B. **A3-C3**: Spike rate at the f_R plotted against f_B. Dots in blue areas indicate simulations where the f_R spike rate is increased compared to f_B (i.e. consistent with phase advances), and dots in red areas indicate simulations where the f_R spike rate is decreased compared to f_B (i.e. consistent with phase delays).

near the inhibitory input frequency. These tests were also performed using MS inputs alone (not shown), which have larger IPSC amplitudes, and similar results are obtained.

In contrast, OLM cell spike resonance due to excitatory PYR cell inputs is consistently in the 2-15 Hz input frequency range, regardless of baseline spike frequency (**Fig. 5B1-B2**). However, the magnitude of the spike resonance is dependent on baseline spike frequency, with larger baseline spike frequencies having smaller spike resonances (**Fig. 5B1**). In all cases the presence of excitatory inputs causes increases in spike rates, which is consistent with phase advances (**Fig. 5B3**). Similar findings are seen when including all input populations (**Fig. 5C1-C3**), suggesting that theta frequency (3-12 Hz) spike resonance *in vitro* is largely dictated by excitatory inputs when they are present and not so much inhibitory inputs alone. We note that our use of a lower number of PYR cell synapses could affect these results, but not likely in a drastic way given that PYR cell entrainment is not sensitive to the number of synapses (see **Fig. 1C**).

Simulated in vivo states have theta frequency spike resonance only for inhibitory inputs

We have previously simulated synaptic bombardment conditions on OLM cells that may be present during *in vivo*-like (IVL) states [see Methods and Guet-McCreight and Skinner (2020)]. This includes a random spread of synaptic locations from different input populations (**Fig. 6A**). In **Fig. 6B** we show what the OLM cell firing looks like under these baseline IVL conditions. We now investigate I-S3 cell control over OLM cells during these IVL states. Since we have already investigated I-S3 cell control over OLM cells in an *in vitro* context, we are able to compare whether or not the same level of control over OLM cell spiking might apply *in vivo*.

We perform the same spike resonance tests as in **Fig. 5**, but now under this IVL state. We see across all input population

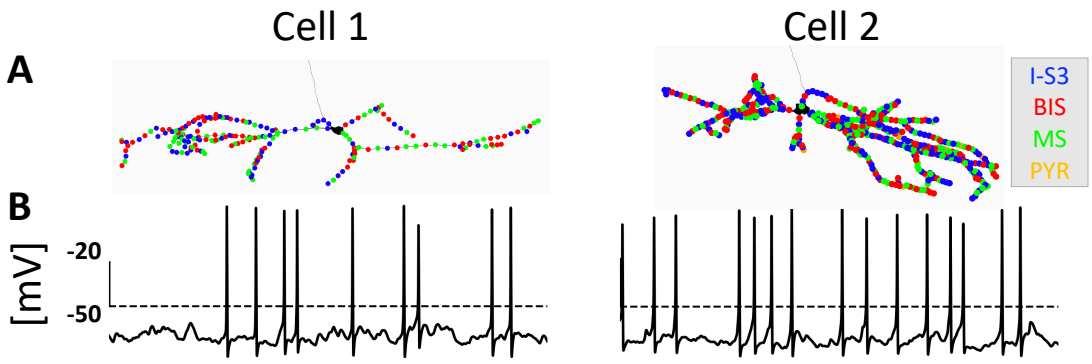

Figure 6. Representative OLM cell firing during an *in vivo*-like state. Input parameters are given in the methods. **A:** Example synaptic locations from the four different input populations with colors as indicated. Note that most of the axonal sections are not shown in these plots and the synaptic location dots on the shape plots are overlaid so some dots may appear less visible than others if they were plotted first (e.g. the PYR cell inputs). **B:** Voltage traces during example IVL states for cell 1 and cell 2.

types (I-S3 cells, PYR cells, and all input populations together) that there is a rightward shift in the resonant frequency distributions towards higher values where more if not all f_R values are larger than the f_B values (**Fig. 7A1-C1 & A2-C2**). That is, even when considering the smaller range of the baseline spike rates, the resonant frequencies are shifted towards higher input frequency ranges. We note that, as in the *in vitro* case, there is no change in the suppressing effects of inhibitory inputs (i.e. PIR spiking remains absent) or the excitable effects of PYR cell inputs on spike rates (**Fig. 7A3-C3**; though note that cell 1 with inputs from all populations can now occasionally cause phase delays instead of phase advances). The shift towards higher f_R values than in the *in vitro* case (i.e. **Fig. 5A2-C2** vs. **Fig. 7A2-C2**) is possibly because of different aspects associated with the IVL state, including more irregular spiking patterns (i.e. spiking is no longer periodic; **Fig. 6B**), as well as a reduction in sensitivity due to a decrease in input resistance. In other words, irregular spike patterns at baseline can allow larger variabilities in f_R values, depending on how spike times align with modulatory excitatory and inhibitory inputs, and decreased input resistance can increase the magnitude of excitatory and inhibitory currents needed to modulate the cell models (i.e. increased f_R values).

Also, when considering the amplitudes of the baseline ratios, the IVL magnitudes (**Fig. 7A1-C1**) are considerably smaller than in the *in vitro* baseline ratios (**Fig. 5A1-C1**). This observation could also be due to an increase in currents in the model once it is put into an IVL state, which generates a lower input resistance and decreased sensitivity to rhythmically-timed inputs. In other words, higher input frequencies will be necessary to elicit spike resonance since there is a decrease in sensitivity. We note that we have previously established that the addition of synaptic bombardment leads to decreases in sensitivity to additional inputs (Guet-McCreight and Skinner, 2019), so it is not surprising that spiking resonance in OLM cells will be different during IVL states.

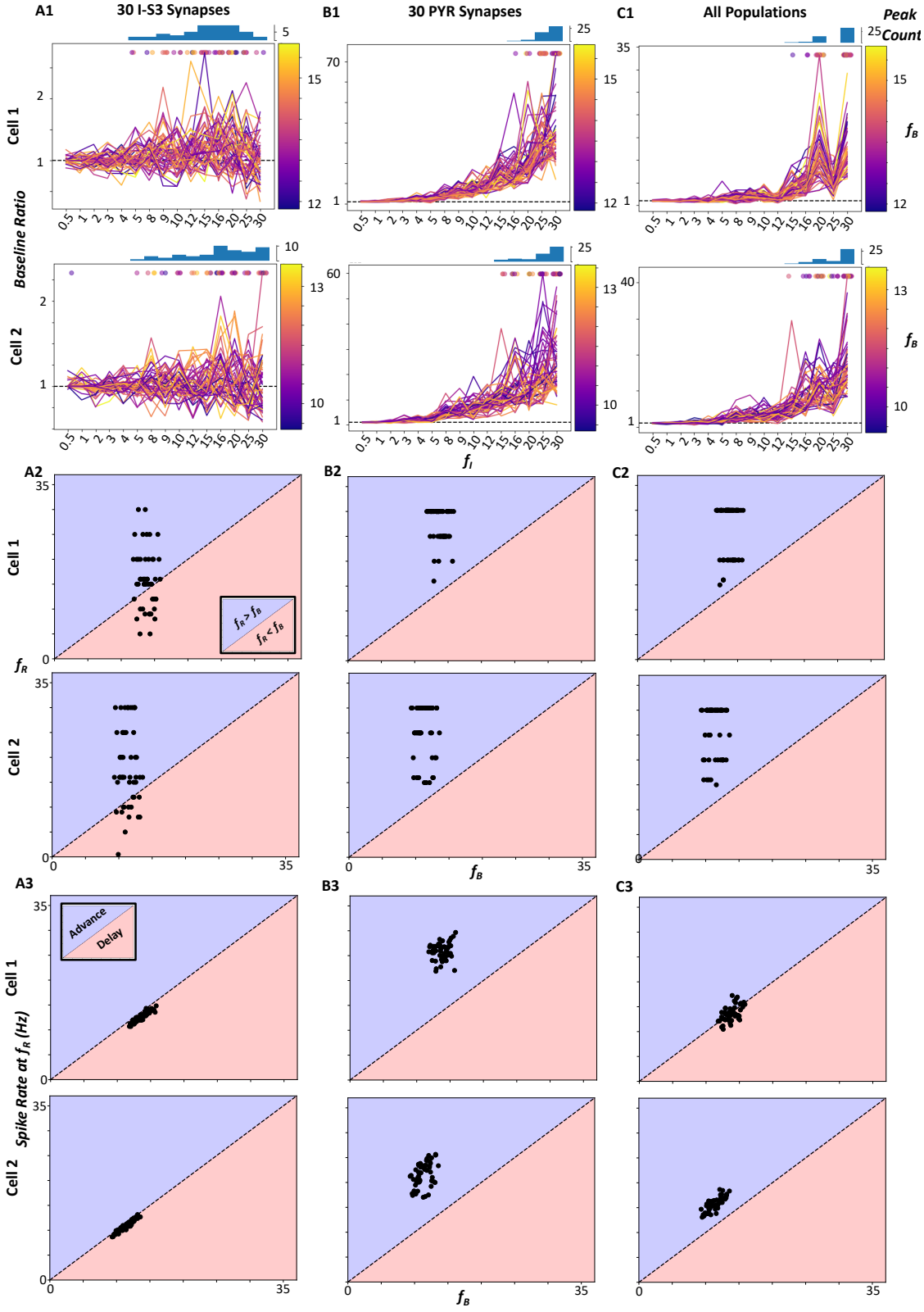

Figure 7. ***In vivo*** **spike resonant frequency of OLM cells are in theta frequency ranges only for inhibitory inputs.**

(Continued) A1-C1: Baseline ratio measurements across types of inputs (**A:** I-S3 cells, **B:** PYR cells, **C:** a combination of all inputs) during simulated *in vivo* states. Baseline ratios computed across different modulation frequency inputs (x-axis) and different IVL synaptic re-randomizations (as shown by the range of different baseline frequencies, f_B indicated by the colorbar). The colored dots plotted above the traces indicate the peak/resonant frequency (the color corresponds to the f_B) and the histograms above the plots show the distributions of peak/resonant frequencies across random seeds and input frequencies. The dashed black lines indicate a baseline ratio of 1, i.e. the point at which the PSD before and after applying modulatory inputs does not change. Values larger than 1 indicate an increase in power, and values smaller than 1 indicate a decrease in the PSD. **A2-C2**: Resonant frequencies, f_R, plotted against f_B. Dots in blue areas indicate simulations where f_R is greater than f_B, and dots in red areas indicate simulations where f_R is less than f_B. **A3-C3**: Spike rate at the f_R plotted against f_B. Dots in blue areas indicate simulations where the f_R spike rate is increased compared to f_B (i.e. consistent with phase advances), and dots in red areas indicate simulations where the f_R spike rate is decreased compared to f_B (i.e. consistent with phase delays). Note that x and y axis scales are chosen to match the same scales as in **Fig. 5A2-C2 & A3-C3** for comparison purposes.

The results between the two OLM cell models are qualitatively similar, despite differences in morphologies and intrinsic parameters. One potential reason for this is the presence of dendritic I_H, and dendritic Na^+ and K^+ channels in both models, which would promote similar integration of synaptic inputs and action potential propagation and thus generate qualitatively similar results across both models. As well, our simulation results are quite similar between using I-S3 cell inputs or MS inputs (not shown), the latter of which have larger IPSC amplitudes (Chamberland et al., 2010). Indeed, there would not be a strict differentiation of incoming inhibitory inputs as modelled in these virtual networks.

Ramp-up of I-S3 cell inputs during theta (8 Hz) modulation can sharpen and modulate OLM cell recruitment

In previous work we found that I-S3 cells are activated with a delay relative to theta-run epochs and spike during the rising to peak phases of theta rhythms (Luo et al., 2020). As well, it was predicted from modelling work that the timing of this phasic preference would be modulated by inputs from entorhinal cortex (EC; rising phase) and CA3 (peak phase). As such, in this section we investigate the effects of a ramp-up of I-S3 cell activation (i.e. simulating a delay in I-S3 cell activation) on a per theta cycle basis during an ongoing theta rhythm (schematized in **Fig. 8**). We run simulations using the full IVL scenarios + 8 Hz modulatory inputs from all input population (I-S3, MS, BIS, and PYR cells) as seen previously (30 synapses per population; **Fig. 7, All Populations**). As before, we add a small amount of noise in all of the theta-timed inputs, as this is both more realistic than having perfectly-timed inputs, and was shown to enhance theta recruitment (Luo et al., 2020). As schematized in **Fig. 8**, starting at 2 s into the simulations until the end of the simulation (10 s), we add 7 I-S3 cell input spikes per cycle, which essentially ramps up the inhibition from I-S3 cells gradually. To consider possible shifts in balances of inputs from CA3 and EC, which can present a possible

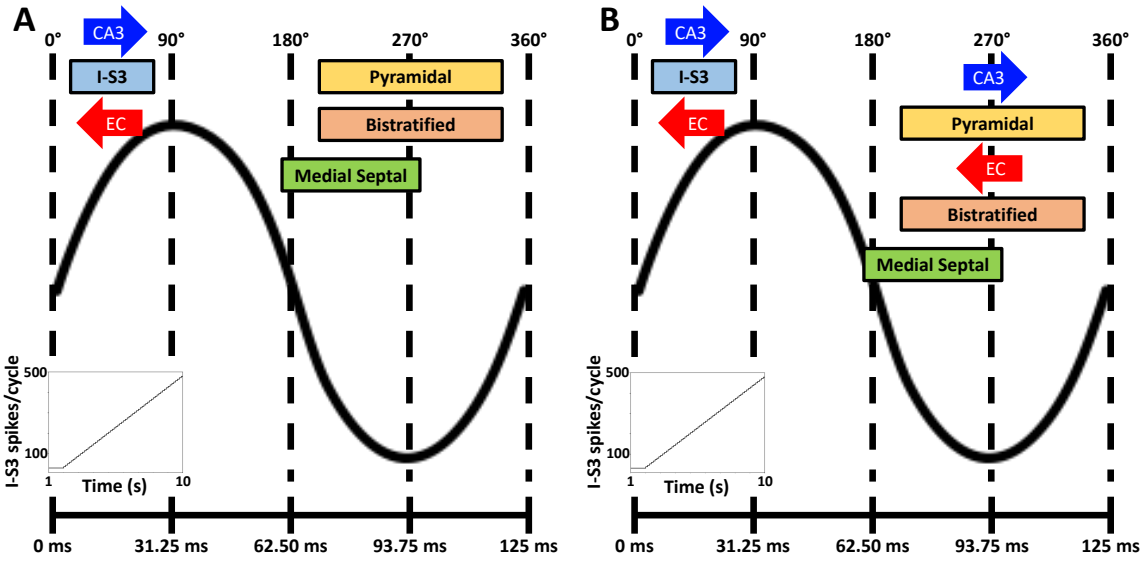

Figure 8. Relative timing of different inputs to OLM cells during a theta cycle. Schematic of simulations where, on top of IVL inputs, we add theta-timed inputs, a ramp-up of I-S3 cell inputs as each simulation progresses (depicted in the bottom-left subplots) as well as either CA3 (+15.625°) or EC (-15.625°) -modulated shifts in the timing of different input populations. **A:** In the first case we impose a shift in the timing of I-S3 cell inputs alone as I-S3 cell inputs are ramped up. **B:** In the second case we impose shifts in the timing of both I-S3 cell inputs as well as PYR cell inputs as I-S3 cell inputs are ramped up.

dis-inhibitory circuitry for switching between sensory inputs and memory consolidation inputs, we also explore shifts in the timing of I-S3 cell inputs alone (**Fig. 8A**) or together with a shift in the timing of PYR cell inputs (**Fig. 8B**). Note that synaptic location sites are chosen randomly for each addition, as described previously (Guet-McCreight and Skinner, 2019). The rationale behind these simulations is that the majority of I-S3 cell activation occurs near run ends, with a delay relative to the timing of activation of other neuron types during theta-run epochs, and so we want to see the effect of a ramp-up of I-S3 cell inputs to OLM cell spiking during a behavioural context with ongoing theta rhythms. Here we use five different random seeds for IVL synapses (of which one of the random seeds is shown in **Fig. 9**), where IVL synapse locations and spike times are re-randomized.

In the simulations where we shift the timing of I-S3 cell inputs alone, the theta-timing of the OLM cell models do not change across any of the conditions (i.e. no ramp-up, stronger EC inputs, even EC/CA3 inputs, or stronger CA3 inputs; **Fig. 9A1 & A3**). We do see a moderate decrease in the spike rate (**Fig. 9B1 & B3**), and an increase in the 8 Hz power in the PSD (**Fig. 9C1 & C3**), across all conditions. More specifically, the enhancement in the PSD is strongest when the timing of the I-S3 cell inputs is shifted towards the peak, corresponding with stronger inputs from CA3 (**Fig. 9C1 & C3**). This appears to be because inhibition occurring following the peak of theta is the most out-of-phase

with the trough of theta, which is when the OLM cell models spike, due to excitation from local PYR cells inputs (**Fig. 9A1 & A3**). Moreover, this also corresponds to the time at which the I-S3 cell inputs will, on average, be most out-of-phase with the OLM cell spike refractory period, which can allow a stronger response to inhibition (**Fig. 4**). As such, I-S3 cell inputs alone can sharpen OLM cell recruitment at theta frequencies by suppressing spikes that are out-of-phase with the theta-timing of OLM cell spiking. We note that when tested across five different random seeds, these same results are generated consistently (i.e. the effect of ramped up I-S3 cell inputs causing spike suppression, and the strongest 8 Hz power when modulated by CA3).

In the simulations where we shift the timing of I-S3 cell inputs together with PYR cell inputs, the theta-timing of the OLM cell models are shifted by the same phasic amount (**Fig. 9A2 & A4**). The interpretation in these simulations is that a shift in the timing of I-S3 cells due to inputs from either EC or CA3 will shift the dis-inhibitory window for PYR cells, and as such, their phasic timing will shift by the same amount. In these simulations we show that this network effect would also shift the timing of OLM cell spiking. Moreover, since the out-of-phase timing is relative to the phasic timing of when the OLM cell models are spiking, we see a similar PSD magnitude at 8 Hz regardless of the direction in which I-S3 and PYR cell inputs are shifted (**Fig. 9C2 & C4**). As well, the spike rates are again moderately decreased when compared to baseline (**Fig. 9B2 & B4**). Again, when tested across five different random seeds, the same results were generated consistently.

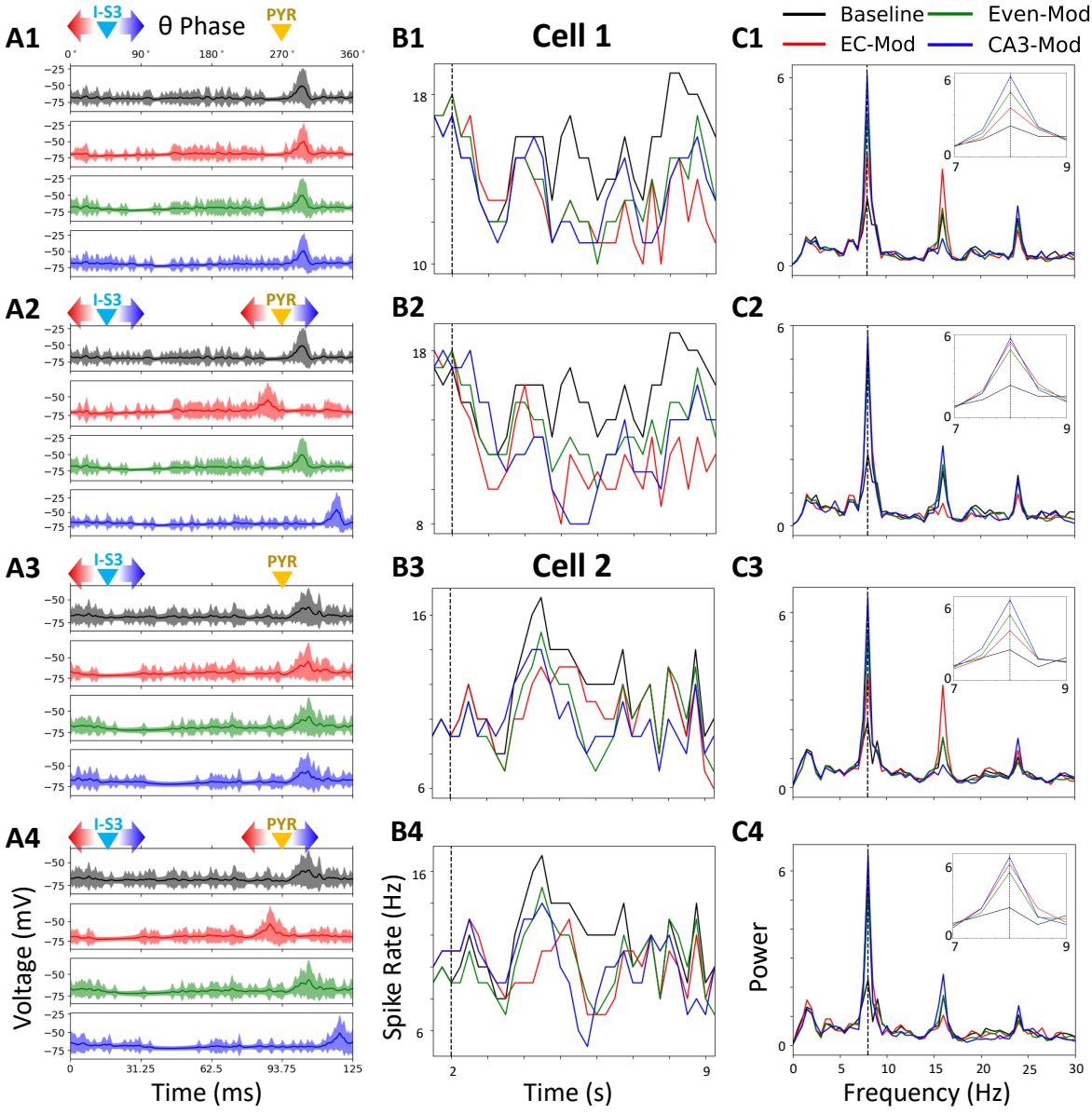

Figure 9. Ramping up I-S3 cell inputs can sharpen and modulate OLM cell recruitment. For each cell model (cell 1 = top 2 rows; cell 2 = bottom 2 rows), we investigate possible scenarios of OLM cell modulation via shifts in the timing of I-S3 and PYR cell inputs based on the timing of CA3 (blue) and EC (red) inputs (Luo et al., 2020). More specifically we look at the condition where the timing of I-S3 cell inputs are modulated on their own (panels A1-C1 & A3-C3), versus where the timing of I-S3 cell inputs are modulated together with the timing of PYR cell inputs (panels A2-C2 & A4-C4). **A:** Plots of the simulated OLM cell model voltage traces averaged across theta cycles. From top to bottom, these plots show the model simulations without a ramp-up (black), with an I-S3 cell ramp-up near the rising phase (red; i.e. stronger CA3 inputs), with an I-S3 cell ramp-up between the rising and peak phases (green; i.e. even inputs from CA3 and EC), as well as with an I-S3 cell ramp-up near the peak phase (blue; i.e. stronger EC inputs), while it is being modulated by 8 Hz frequency inputs from all input population types.

(Continued) To generate these average traces, we take the voltage traces (1,000 to 10,000 ms), split them each into their 72 theta cycles (i.e. $9000\ ms/125\ ms = 72\ cycles$), and then compute the average 125 ms theta cycle traces. Shaded areas show the amount of standard deviation above or below the mean. **B:** Resulting suppression on the spike rate of the OLM cell model throughout the simulations. **C:** The PSD of the voltage traces before and after applying a ramp-up of I-S3 cell inputs. The inset plot shows the magnified PSD between 7 to 9 Hz. Note that all simulations shown in this plot are performed using the same random seed for IVL synapse locations and IVL presynaptic spike times.

Discussion

Mapping identified inhibitory cell types to function and behaviour is a challenging endeavour. To address this, we took advantage of our previous studies interfacing experiment with modeling work of inhibitory cell types in the hippocampus. We focused on how specialized interneuron-selective cells, I-S3 cells, might exert their influence over OLM cells that have a demonstrated gating control between incoming 'sensory' and ongoing 'memory' information flow. We used two OLM cell models with parameters fit according to experimental data obtained from the same cell, populations of synapses with parameters specific to cell types that synapse onto OLM cells, knowledge of I-S3 cell firing *in vivo*, as well as a methodology for generating *in vivo*-like states.

How do I-S3 cells control OLM cell spiking in vivo?

Starting from the *in vitro* experimental observation of Tyan et al. (2014) in which OLM cells possibly exhibit PIR due to I-S3 cell inhibitory inputs, we considered two other possibilities. From simulated *in vitro* considerations, we found that I-S3 cell-mediated disinhibition of pyramidal cells seemed most likely to be the way in which I-S3 cells would exert their influence on OLM cell spike timing. I-S3 cell-mediated suppression of OLM cells would be part of enabling this contribution, but *not* PIR mechanisms. BIS cells could also contribute in these interactions. Thus, based on our explorations, we predict that the influence that I-S3 cells would have on OLM cells would be through spike suppression followed by enhanced excitation of OLM cells due to PYR cell disinhibition.

Interestingly, when simulating *in vivo* states in OLM cells, only inhibitory inputs, that would include those from I-S3 cells, could lead to a spike resonance at theta frequencies. This was not the case during simulation of *in vitro* states though - there it was excitatory and not inhibitory inputs that could lead to theta frequency spike resonances. In previous modeling work, it was found that OLM cell spike resonance with inhibitory inputs in simplified, simulated *in vivo* states could occur at high or low theta frequencies depending on whether dendritic h-channels were present or not, respectively (Sekulić and Skinner, 2017). Here, we used our state-of-the-art OLM cell models that were shown to necessarily have dendritic h-channels (Sekulic et al., 2020), a different metric for gauging spike resonance (i.e. the maximal baseline ratio), a series of different baseline spike rates [i.e. instead of just 2.5 Hz, as in Sekulić and Skinner (2017)], and synaptic parameters estimated from actual input populations measured experimentally. Based on the results here, we predict that theta frequency spike resonance could occur in OLM cells *in vivo* with incoming inhibitory I-S3 cell inputs, as well as from other rhythmic inhibitory inputs like MS and BIS cell inputs.

From previous work, we know that I-S3 cells exhibit a delay relative to theta-run epochs, with a phasic preference towards the rising/peak phases of theta. Simulating a ramp-up of I-S3 cell spiking in our virtual networks, we found that we could obtain a sharpening of the timing of OLM cells during theta rhythms, which could contribute to shaping pyramidal cell place fields (Royer et al., 2012). In fact, silencing SOM+ cells increases PYR cell burst spiking during

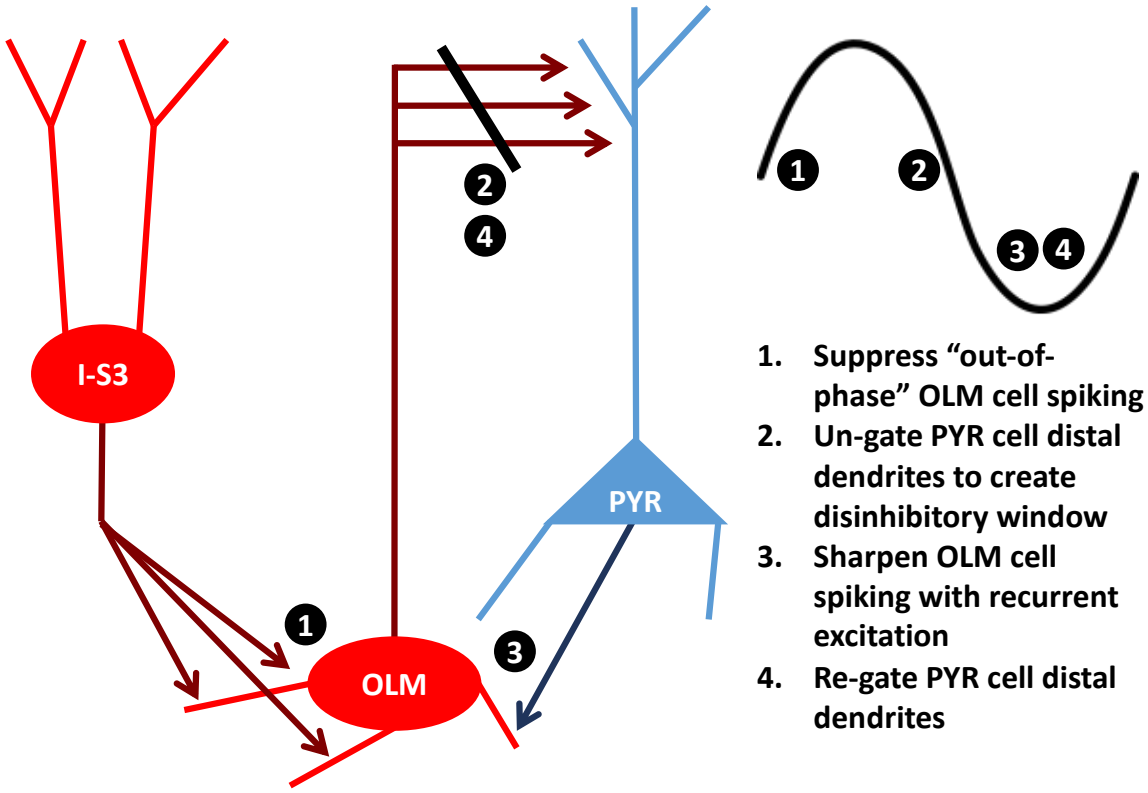

Figure 10. I-S3 cells are fit to suppress OLM cell spiking and disinhibit pyramidal cells.

place field traversals in awake mice (Royer et al., 2012), and also ungates synaptic activation along pyramidal cell apical dendrites (Lovett-Barron et al., 2012). In line with this, optogenetic silencing of VIP+ cells, which promotes activation of SOM+ cells, dampens both the reshaping of PYR cell place fields and learning of reward site locations (Turi et al., 2019). Previous modeling has also shown that OLM cells, via network pathways that include BIS cells, were key to LFP signal robustness of ongoing intrinsic theta rhythms (Chatzikalymniou and Skinner, 2018). Thus, I-S3 cell contributions, via OLM and BIS cells, could be essential for the existence of robust theta rhythms.

Based on all of this, our proposition for I-S3 cell contributions is illustrated in **Fig. 10** in a series of steps. We predict that I-S3 cells cause phase delays in OLM cell spiking by spike suppression, as opposed to PIR-mediated phase advances (step 1). This would lead to PYR cell spiking due to disinhibition at a particular phase of theta rhythms (step 2), which would subsequently dictate the timing of the OLM cell spiking through excitation (step 3), leading to re-gating of inputs at distal dendrites (step 4).

Experimental Investigations

The predictions from our computational studies lead to several suggestions for experimental investigation. Results from Tyan et al. (2014) can be re-tested by performing frequency-modulated optogenetic stimulation of CR+ cells while recording from OLM cells in the presence of excitatory synaptic blockers. If OLM cell frequency-modulated spiking is then lost, the interpretation would be that the frequency modulation was due to feedforward disinhibition-driven excitation onto OLM cells. Additionally, instead of recording from OLM cells during these tests, one could record from PYR cells to verify frequencies at which I-S3 cell activation might lead to disinhibited spiking in PYR cells, if at all.

Another suggestion would be to perform closed-loop feedback stimulation with the theta-filtered LFP as has been done previously (Siegle and Wilson, 2014), but with photo-activation of CR+ cells at specific phases of theta. One could stimulate CR+ cells at phases closer to the peak versus the trough of theta, to assess whether the phasic timing of CR+ cells has an effect on the encoding and retrieval of information during a learning test such as the T-maze task. Our results predict an ungating of pyramidal cells during theta phases that follow the activation of CR+ cells. On average (but with a large variance), I-S3 cells spike near the rising to peak phases of theta (Luo et al., 2020) which follows excitation from EC and precedes excitation from CA3. As such, if stimulated to spike at earlier phases, integration of inputs from EC by pyramidal cells could be favoured to promote sensory encoding. Likewise, if stimulated to spike at later phases, integration of inputs from CA3 by pyramidal cells could be favoured to promote retrieval of information.

Further, it is now clear that the location of OLM cells along the dorsoventral axis of the hippocampus matters in terms of whether one has high or low theta rhythms (Hilscher et al., 2019; Mikulovic et al., 2018; Siwani et al., 2018), since there may be biophysical and connectivity differences with OLM cells in these different locations. As already noted above, modeling studies have suggested that whether h-channels are present or not in the dendrites of OLM cells could 'control' the theta frequency spike resonance. Here, we used OLM cell models with dendritic h-channels developed from intermediate CA1 mouse hippocampal data (Sekulic et al., 2020), and our PRC explorations indicated that current changes with inhibitory perturbations were mostly due to h-channels.

Theoretical and Modeling Considerations

To examine the ability of OLM cells to exhibit phase advances or delays with inhibitory perturbations, we used PRCs but with noted differences from theoretical PRC studies that typically consider a square-pulse stimulation and use single compartment models. Here we have detailed multi-compartment models with a full suite of biophysical channel types. Since we wanted to situate our explorations in a realistic biological setting, our inhibitory perturbations took the form of dendritically distributed inhibitory synaptic inputs on the OLM cell models with synaptic features estimated from experiment. These PRCs serve as an approximation for how OLM cells would respond to repeated 'periodic

forcing' (Rinzel and Ermentrout, 1989), and they show that incoming inhibitory inputs mostly serve to slow down the firing of OLM cells. Moreover, by also examining the underlying changes in the biophysical currents of OLM cells, we found that h-channel changes dominate, but they are not sufficient to lead a phase advance rather than a phase delay.

To allow a focus on cellular details, we carried out virtual network explorations. This allowed us to directly compare and translate *in vitro* aspects to *in vivo* to come up with our proposed specialized contribution of I-S3 cells. Since *in vivo* recordings of specialized cell types is highly challenging, computational studies to develop hypotheses, predict and guide experimental studies are strongly needed. However, a virtual network does not directly model all of the interacting network effects that can occur consequentially as a result of changes in the activation of the cell type of interest. Despite these properties not being modelled explicitly, this approach offers the benefit of being able to dissect out putative mechanisms without having to build a full-blown circuit model initially. We also note that our interpretations are in line with previous network modelling showing that VIP/SOM connectivity is sufficient for switching circuit activity between two processing modes where synaptic inputs in pyramidal cells are either integrated or suppressed (Hertäg and Sprekeler, 2019; Wang et al., 2004; Yang et al., 2016).

References

Acsády L, Görcs TJ, Freund TF (1996) Different populations of vasoactive intestinal polypeptide-immunoreactive interneurons are specialized to control pyramidal cells or interneurons in the hippocampus. *Neuroscience* 73:317–334.

Ascoli GA, Gasparini S, Medinilla V, Migliore M (2010) Local Control of Postinhibitory Rebound Spiking in CA1 Pyramidal Neuron Dendrites. *Journal of Neuroscience* 30:6434–6442.

Bezaire MJ, Raikov I, Burk K, Vyas D, Soltesz I (2016) Interneuronal mechanisms of hippocampal theta oscillations in a full-scale model of the rodent CA1 circuit. *eLife* 5:e18566.

Bezaire MJ, Soltesz I (2013) Quantitative assessment of CA1 local circuits: Knowledge base for interneuron-pyramidal cell connectivity. *Hippocampus* 23:751–785.

Buzsáki G (2002) Theta Oscillations in the Hippocampus. *Neuron* 33:325–340.

Carnevale NT, Hines ML (2006) *The NEURON Book* Cambridge University Press, Cambridge, UK ; New York, 1 edition edition.

Cembrowski MS, Spruston N (2019) Heterogeneity within classical cell types is the rule: lessons from hippocampal pyramidal neurons. *Nature Reviews Neuroscience* 20:193.

Chamberland S, Salesse C, Topolnik D, Topolnik L (2010) Synapse-Specific Inhibitory Control of Hippocampal Feedback Inhibitory Circuit. *Frontiers in Cellular Neuroscience* 4.

Chamberland S, Topolnik L (2012) Inhibitory control of hippocampal inhibitory neurons. *Frontiers in Neuroscience* 6.

Chatzikalymniou AP, Skinner FK (2018) Deciphering the Contribution of Oriens-Lacunosum/Moleculare (OLM) Cells to Intrinsic Theta Rhythms Using Biophysical Local Field Potential (LFP) Models. *eNeuro* pp. ENEURO.0146–18.2018.

Colgin LL (2016) Rhythms of the hippocampal network. *Nature Reviews Neuroscience* 17:239–249.

Francavilla R, Villette V, Luo X, Chamberland S, Muñoz-Pino E, Camiré O, Wagner K, Kis V, Somogyi P, Topolnik L (2018) Connectivity and network state-dependent recruitment of long-range VIP-GABAergic neurons in the mouse hippocampus. *Nature Communications* 9:5043.

Guet-McCreight A, Skinner FK (2019) Using computational models to predict in vivo synaptic inputs to interneuron specific 3 (IS3) cells of CA1 hippocampus that also allow their recruitment during rhythmic states. *PLOS ONE* 14:e0209429.

Guet-McCreight A, Skinner FK (2020) Computationally going where experiments cannot: a dynamical assessment of dendritic ion channel currents during in vivo-like states. *F1000Research* 9:180.

Guet-McCreight A, Skinner FK, Topolnik L (2020) Common Principles in Functional Organization of VIP/Calretinin Cell-Driven Disinhibitory Circuits Across Cortical Areas. *Frontiers in Neural Circuits* 14 Publisher: Frontiers.

Hangya B, Borhegyi Z, Szilágyi N, Freund TF, Varga V (2009) GABAergic Neurons of the Medial Septum Lead the Hippocampal Network during Theta Activity. *Journal of Neuroscience* 29:8094–8102.

Harris KD, Hochgerner H, Skene NG, Magno L, Katona L, Gonzales CB, Somogyi P, Kessaris N, Linnarsson S, Hjerling-Leffler J (2018) Classes and continua of hippocampal CA1 inhibitory neurons revealed by single-cell transcriptomics. *PLOS Biology* 16:e2006387.

Hertäg L, Sprekeler H (2019) Amplifying the redistribution of somato-dendritic inhibition by the interplay of three interneuron types. *PLOS Computational Biology* 15:e1006999.

Hilscher MM, Nogueira I, Mikulovic S, Kullander K, Leão RN, Leão KE (2019) Chrna2-OLM interneurons display different membrane properties and h-current magnitude depending on dorsoventral location. *Hippocampus* .

Katona L, Lapray D, Viney TJ, Oulhaj A, Borhegyi Z, Micklem BR, Klausberger T, Somogyi P (2014) Sleep and Movement Differentiates Actions of Two Types of Somatostatin-Expressing GABAergic Interneuron in Rat Hippocampus. *Neuron* 82:872–886.

Kepecs A, Fishell G (2014) Interneuron cell types are fit to function. *Nature* 505:318–326.

Kispersky TJ, Fernandez FR, Economo MN, White JA (2012) Spike Resonance Properties in Hippocampal O-LM Cells Are Dependent on Refractory Dynamics. *The Journal of Neuroscience* 32:3637–3651.

Klausberger T, Somogyi P (2008) Neuronal Diversity and Temporal Dynamics: The Unity of Hippocampal Circuit Operations. *Science* 321:53–57.

Leão RN, Mikulovic S, Leão KE, Munguba H, Gezelius H, Enjin A, Patra K, Eriksson A, Loew LM, Tort ABL, Kullander K (2012) OLM interneurons differentially modulate CA3 and entorhinal inputs to hippocampal CA1 neurons. *Nature Neuroscience* 15:1524–1530.

Lovett-Barron M, Turi GF, Kaifosh P, Lee PH, Bolze F, Sun XH, Nicoud JF, Zemelman BV, Sternson SM, Losonczy A (2012) Regulation of neuronal input transformations by tunable dendritic inhibition. *Nature Neuroscience* 15:423–430.

Luo X, Guet-McCreight A, Villette V, Francavilla R, Marino B, Chamberland S, Skinner FK, Topolnik L (2020) Synaptic Mechanisms Underlying the Network State-Dependent Recruitment of VIP-Expressing Interneurons in the CA1 Hippocampus. *Cerebral Cortex* .

Maccaferri G, McBain CJ (1996) The hyperpolarization-activated current (Ih) and its contribution to pacemaker activity in rat CA1 hippocampal stratum oriens-alveus interneurones. *The Journal of Physiology* 497:119–130.

Markram H, Toledo-Rodriguez M, Wang Y, Gupta A, Silberberg G, Wu C (2004) Interneurons of the neocortical inhibitory system. *Nature Reviews Neuroscience* 5:793.

Mikulovic S, Restrepo CE, Siwani S, Bauer P, Pupe S, Tort ABL, Kullander K, Leão RN (2018) Ventral hippocampal OLM cells control type 2 theta oscillations and response to predator odor. *Nature Communications* 9:3638.

Mizuseki K, Sirota A, Pastalkova E, Buzsáki G (2009) Theta Oscillations Provide Temporal Windows for Local Circuit Computation in the Entorhinal-Hippocampal Loop. *Neuron* 64:267–280.

Pelkey KA, Chittajallu R, Craig MT, Tricoire L, Wester JC, McBain CJ (2017) Hippocampal GABAergic Inhibitory Interneurons. *Physiological Reviews* 97:1619–1747.

Rinzel J, Ermentrout GB (1989) Analysis of neural excitability and oscillations In Koch C, Segev I, editors, *Methods in Neuronal Modeling*, pp. 135–169. MIT Press, Cambridge, MA, USA.

Royer S, Zemelman BV, Losonczy A, Kim J, Chance F, Magee JC, Buzsáki G (2012) Control of timing, rate and bursts of hippocampal place cells by dendritic and somatic inhibition. *Nature Neuroscience* 15:769–775.

Schultheiss NW, Prinz AA, Butera RJ, editors (2011) *Phase Response Curves in Neuroscience: Theory, Experiment, and Analysis* Springer, New York, 2012 edition edition.

Sekulic V, Yi F, Garrett T, Guet-McCreight A, Lawrence JJ, Skinner FK (2020) Integration of within-cell experimental data with multi-compartmental modeling predicts h-channel densities and distributions in hippocampal OLM cells. *Frontiers in Cellular Neuroscience* 14 Publisher: Frontiers.

Sekulić V, Skinner FK (2017) Computational models of O-LM cells are recruited by low or high theta frequency inputs depending on h-channel distributions. *eLife* 6:e22962.

Siegle JH, Wilson MA (2014) Enhancement of encoding and retrieval functions through theta phase-specific manipulation of hippocampus. *eLife* 3:e03061.

Sivagnanam S, Majumdar A, Yoshimoto K, Astakhov V, B A, Martone M, Carnevale NT (2013) *Introducing The Neuroscience Gateway*, Vol. 993 of CEUR Workshop Proceedings of *CEUR Workshop Proceedings*.

Siwani S, França ASC, Mikulovic S, Reis A, Hilscher MM, Edwards SJ, Leão RN, Tort ABL, Kullander K (2018) OLMα2 Cells Bidirectionally Modulate Learning. *Neuron* 99:404–412.e3.

Tremblay R, Lee S, Rudy B (2016) GABAergic Interneurons in the Neocortex: From Cellular Properties to Circuits. *Neuron* 91:260–292.

587 Turi GF, Li WK, Chavlis S, Pandi I, O'Hare J, Priestley JB, Grosmark AD, Liao Z, Ladow M, Zhang JF, Zemelman
588 BV, Poirazi P, Losonczy A (2019) Vasoactive Intestinal Polypeptide-Expressing Interneurons in the Hippocampus
589 Support Goal-Oriented Spatial Learning. *Neuron* 101:1150–1165.e8.

590 Tyan L, Chamberland S, Magnin E, Camiré O, Francavilla R, David LS, Deisseroth K, Topolnik L (2014) Dendritic
591 Inhibition Provided by Interneuron-Specific Cells Controls the Firing Rate and Timing of the Hippocampal Feedback
592 Inhibitory Circuitry. *Journal of Neuroscience* 34:4534–4547.

593 Varga C, Golshani P, Soltesz I (2012) Frequency-invariant temporal ordering of interneuronal discharges during
594 hippocampal oscillations in awake mice. *Proceedings of the National Academy of Sciences* 109:E2726–E2734.

595 Wang XJ, Tegnér J, Constantinidis C, Goldman-Rakic PS (2004) Division of labor among distinct subtypes
596 of inhibitory neurons in a cortical microcircuit of working memory. *Proceedings of the National Academy of*
597 *Sciences* 101:1368–1373.

598 Yang GR, Murray JD, Wang XJ (2016) A dendritic disinhibitory circuit mechanism for pathway-specific gating.
599 *Nature Communications* 7:1–14.

600 Zemankovics R, Káli S, Paulsen O, Freund TF, Hájos N (2010) Differences in subthreshold resonance of hippocampal
601 pyramidal cells and interneurons: the role of h-current and passive membrane characteristics. *The Journal of*
602 *Physiology* 588:2109–2132.

603 Zeng H, Sanes JR (2017) Neuronal cell-type classification: challenges, opportunities and the path forward. *Nature*
604 *Reviews Neuroscience* 18:530.

605 Figure Legends

606 **Figure 1 Potential mechanisms through which I-S3 cell activation can control OLM cell spiking.**

607

608 **Figure 2 Example locations of synaptic inputs.**

609

610 **Figure 3 I-S3 cell inputs alone cannot elicit PIR spiking in OLM cells at higher-than-baseline spike rate**
611 **frequencies.**

612

613 **Figure 4 Inhibitory perturbations alone mostly just cause phase delays in OLM cell models.**

614

615 **Figure 5 *In vitro* spike resonant frequency of OLM cell models due to inhibitory inputs, but not excitatory**
616 **inputs, is dependent on the baseline spike rate.**

617

618 **Figure 6 Representative OLM cell firing during an *in vivo*-like state.**

619

620 **Figure 7 *In vivo* spike resonant frequency of OLM cells are in theta frequency ranges only for inhibitory inputs.**

621

622 **Figure 8 Relative timing of different inputs to OLM cells during a theta cycle.**

623

624 **Figure 9 Ramping up I-S3 cell inputs can sharpen and modulate OLM cell recruitment.**

625

626 **Figure 10 I-S3 cells are fit to suppress OLM cell spiking and disinhibit pyramidal cells.**

627

628